

Multivortex states and dynamics in nonequilibrium quantum fluids

Vladimir N. Gladilin and Michiel Wouters

TQC, Universiteit Antwerpen, Universiteitsplein 1, B-2610 Antwerpen, Belgium

(Dated: October 16, 2018)

In strongly nonequilibrium Bose-Einstein condensates described by the generalized Gross-Pitaevskii equation, vortex motion becomes self-accelerated while the long-range vortex-antivortex interaction appears to be repulsive. We numerically study the impact of these rather unusual vortex properties on the dynamics of multivortex systems. We show that at strong nonequilibrium the repulsion between vortices and antivortices leads to a dramatic slowdown of their annihilation. Moreover, in finite-size samples, relaxation of multivortex systems can lead to the formation of metastable vortex-antivortex clusters, whose shape and size depend, in particular, on the sample geometry, boundary conditions and deviations from equilibrium. We further demonstrate that at strong nonequilibrium the interaction of self-accelerated vortices with inhomogeneous condensate flows can lead to generation of new vortex-antivortex pairs.

PACS numbers: 03.75.Lm, 71.36.+c

I. INTRODUCTION

Topological defects, ubiquitous in ordered phases of matter, ranging from superfluids and superconductors to neutron stars and even cosmology, have been investigated for many decades [1]. Especially noteworthy discoveries have been the Abrikosov vortex lattice, the Berezinskii-Kosterlitz-Thouless (BKT) phase transition in two-dimensional superfluids and the Kibble-Zurek (KZ) mechanism. An Abrikosov vortex lattice is formed when a superfluid is subject to rotation or a superconductor is put in a magnetic field. A large number of vortices is then created and they arrange in a regular lattice because of their repulsive interactions. The BKT mechanism is driven by thermally activated vortex-antivortex pair dissociation, that results in a transition from a superfluid state with quasi-long range order to a normal state. In the KZ mechanism on the other hand, topological defects are created by a rapid quench through the phase transition. They subsequently annihilate on a much longer time scale.

In by far most of the systems that have been investigated, the assumption of (local) thermal equilibrium can be assumed to hold. A natural extension of these studies is then the consideration of ordered systems that are subject to continuous driving and dissipation. An experimental motivation for this question stems from the study of exciton-polariton condensates [2]. In order to compensate for the finite polariton lifetime, excitations have to be continuously injected. This driving and dissipation prevents the system from reaching local equilibrium. At the same time, an out-of-equilibrium system does not imply an unstable system since stability is obtained through the balance of dissipation and gain.

Spurred by these experimental developments [3–7], several theoretical works have analyzed the properties of vortices in polariton condensates [8–10]. A more recent research activity has been devoted to the understanding of the BKT transition out of equilibrium. In one of these works [11], it was numerically found that the usual sce-

nario survives the introduction of driving and dissipation in a finite size system, where the renormalisation group based studies [12, 13] found modifications at large length scales. More recently, it was shown how the different regimes can be reached in a polariton quantum fluid in the parametric oscillation regime [14]. The modification of the transition can be related to a change in the interaction between vortices and antivortices, that can become repulsive at large distances for weak nonequilibrium [12] to entirely repulsive at strong driving and dissipation [15]. This profound change in interaction between vortices of opposite sign can be attributed to radial current flows that are emitted from the vortex cores in a nonequilibrium condensate. Moreover, for stronger nonequilibrium, the vortex motion becomes self-accelerated: a vortex is dragged by its own slowly relaxing flow field.

The rather unusual properties of individual vortices and pairwise vortex interactions, revealed in [15] can be expected not only to affect the BKT transition, but can also lead to the formation of new vortex lattice structures. The existence of such stable complexes could strongly affect the phase ordering kinetics [16] after a KZ quench [17] through the phase transition. Specifically, we will address the following questions in this paper. How are the dynamics of multivortex systems modified as a result of the vortex-antivortex repulsion? Can this repulsion lead to the appearance of metastable vortex-antivortex configurations in pinning-free nonequilibrium condensates, and what are those configurations? What happens with self-accelerated vortices when the deviation from equilibrium further increases? In particular, can a self-accelerated vortex, similarly to a fast moving obstacle, produce new vortex-antivortex pairs, akin to a von Kármán street [18–20])?

The paper is organized as follows. In Sec. II we describe the theoretical model and the numerical scheme used in our calculations. The processes of vortex-antivortex recombination in nonequilibrium polariton condensates are considered in Sec. III. Section IV deals with the formation of various metastable vortex-

antivortex states in finite-size samples. In Sec. V we analyze the effects produced by fast moving vortices in strongly nonequilibrium polariton superfluids. The main conclusions from the obtained results are summarized in Sec. VI.

II. MODEL

We describe the nonresonantly excited two-dimensional polariton condensate by the generalized Gross-Pitaevskii equation that is obtained after adiabatic elimination of the exciton reservoir [21–23]

$$(i - \kappa)\hbar\frac{\partial\psi}{\partial t} = \left[-\frac{\hbar^2\nabla^2}{2m} + g|\psi|^2 + \frac{i}{2}\left(\frac{P}{1 + |\psi|^2/n_s} - \gamma\right) \right] \psi, \quad (1)$$

Here m is the effective mass and the contact interaction between polaritons is characterized by the strength g . The imaginary term in the square brackets on the right hand side describes the saturable pumping (with strength P and saturation density n_s) that compensates for the losses (γ). We take into account that the energy relaxation κ in the condensate [24, 25], may be non-negligible. It originates from scattering with thermal phonons and excitons and results in the appearance of damping in the vortex dynamics. In particular, this damping tends to impede vortex drag by a condensate flow so that the vortex core velocity becomes smaller than the velocity of the surrounding condensate. This results in the appearance of a non-zero Magnus force, exerted on a vortex and perpendicular to the flow direction. Thus, for two vortices of the same (opposite) chirality, moving in each other velocity field, the Magnus forces lead to mutual repulsion (attraction).

With the help of the Madelung transformation $\psi = \sqrt{ne}^{i\theta}$, a continuity equation can be derived for the polariton density n

$$(1 + \kappa^2)\frac{\partial n}{\partial t} + \nabla \cdot (n\mathbf{v}) = (R - 2\kappa\epsilon)n. \quad (2)$$

Here, we introduced the velocity $\mathbf{v} = \nabla\theta/m$, the net gain $R = P/(1 + n/n_s) - \gamma$ and the single particle energy $\epsilon = gn + \frac{m}{2}\mathbf{v}^2 + \frac{\nabla^2\sqrt{n}}{2m\sqrt{n}}$. The right hand side of the continuity equation shows that the net gain acts as a source of particles. The increase of R with decreasing density implies that a particle source is present where the density is locally suppressed, such as at a vortex core or at the sample boundary.

In general, the pumping intensity P is coordinate dependent and can be represented as $P(\mathbf{r}) = P_0p(\mathbf{r})$, with $P_0 = \max P(\mathbf{r})$. Since the interaction strength is positive, $g > 0$, it is convenient to rewrite Eq. (1) in a dimensionless form, by expressing the particle density $|\psi|^2$ in units of $n_0 \equiv n_s(P_0/\gamma - 1)$, time in units of $\hbar/(gn_0)$, and length

in units of $\hbar/\sqrt{2mgn_0}$:

$$(i - \kappa)\frac{\partial\psi}{\partial t} = \left[-\nabla^2 + |\psi|^2 + ic\frac{1 - |\psi|^2 + (1 + \nu^{-1})(p - 1)}{1 + \nu|\psi|^2} \right] \psi. \quad (3)$$

Equation (3) contains three dimensionless scalar parameters: κ characterizes, as described above, damping in the system dynamics, $c = \gamma/(2gn_s)$ is a measure of the deviation from equilibrium, and $\nu = n_0/n_s$ is proportional to the relative excess of the maximum pumping intensity P_0 over the threshold intensity. The dimensionless function $p(\mathbf{r})$ ($0 \leq p \leq 1$) describes the spatial distribution of the pumping intensity.

Equation (3) is solved numerically using a finite-difference scheme. One of the key elements of our approach [26] is the use of automatically adapted time step h_t . The adaptation is aimed at minimizing the number of steps in t and - at the same time - at keeping the solving procedure accurate. This allows us to combine an accurate and detailed description of fast stages in the system dynamics with a high time efficiency in the case when the dynamics is relatively slow. The proposed approach has been successfully applied to describe different kinds of vortex dynamics in superconducting condensates (see, e. g., [27–29]) as well as the motion of vortex-(anti)vortex pairs and individual vortices in nonequilibrium polariton condensates [15]. Here we use a uniform two-dimensional grid with the step $h = 0.2$ to 0.5 . The time step h_t is typically $\sim 10^{-5}$ to 10^{-3} depending on the specific distribution of the order parameter.

Our simulations are performed for infinite periodic systems and finite-size samples. In the latter case we use the Dirichlet boundary conditions $\psi|_{\text{boundary}} = 0$. Due to suppression of the polariton density at the boundary, radiative polariton losses are locally reduced. For this reason, at uniform pumping the boundary becomes a source of extra polaritons, which propagate inside the sample (cp. radial flows emitted by a vortex core [15]). These inward currents tend to drag vortices away from the boundaries, providing an effective confinement for vortices. The strength of this confinement can be tuned by changing the pump intensity near the boundary. In the present calculations we consider the intensity distribution in the form of

$$p(x, y) = 1 - \alpha e^{-d(x, y)/d_0}, \quad (4)$$

where $d(x, y)$ is the distance to the nearest sample boundary and the positive parameter α is smaller than 1. With increasing α and/or d_0 the inward currents weaken and can even turn to outward flows at sufficiently large α . The latter case, where vortices are removed very fast from the sample, impeding the study of vortex dynamics, is not studied in the present work.

III. VORTEX-ANTIVORTEX ANNIHILATION

It is natural to expect that the vortex-antivortex repulsion, caused by the outflow of condensate particles from a vortex core, can significantly affect the processes of vortex-antivortex recombination in non-equilibrium condensates [12, 15]. Vortices in non-equilibrium condensates can emerge in different schemes. Apart from the spontaneous generation of vortices induced by noise [11], vortices can appear due to resonant excitation with a Gauss-Laguerre beam [30, 31], creation of polariton condensates using chiral lenses [32], or by a rapid quench of the pump power, in analogy to the Kibble-Zurek mechanism [17, 33, 34].

After the injection of a certain number of vortices, the subsequent phase healing dynamics typically consists of the annihilation of vortex-antivortex pairs, leading to a decay of the number of vortices [16, 34]. In Fig. 1 we show the calculated time dependence of the number of vortex pairs per unit cell of a periodic system with period $L_x = L_y = 165$. The initial conditions correspond to the presence of 1000 vortices and 1000 antivortices, randomly distributed within the unit cell. At $c = 0.04$, $\nu = 0.06$, and $\kappa = 0.019$ our system practically coincides with one of those analyzed in [34]. Quite in line with the results of [34], for this set of parameters the simulated late-time dynamics closely follows the dependence $N \sim [(t/t_0)/\log(t/t_0)]^{-1}$ with $t_0 = 0.33$. This dynamic does not change too much when the parameter ν considerably increases (see the dashed curve in Fig. 1).

On the other hand, an increase of the nonequilibrium parameter to $c = 1$ results in a dramatic slowing down of the vortex-antivortex annihilation at relatively large t (see the dotted curve for $c = 1$, $\nu = 0.06$, and $\kappa = 0.019$). Like in the case of weak non-equilibrium ($c = 0.04$), the behavior of $N(t)$ at $c = 1$ is rather insensitive to the value of ν (compare the dotted and dash-dotted curves to each other). At the same time, the annihilation processes can be somewhat accelerated by increasing the damping parameter κ (see the dash-dot-dot curve in Fig. 1). As described above, stronger damping enhances the Magnus effect and the corresponding attractive component in the vortex-antivortex interaction. Nevertheless, even for κ as large as 0.2, the average annihilation rate at $c = 1$ is seen to be by orders of magnitude lower than that in the nearly equilibrium system with $c = 0.04$.

Our simulations show that the repulsion between vortices and antivortices can considerably slow down their recombination already at moderate deviations from equilibrium. Figure 2 illustrates this effect for the more experimentally relevant case of a finite-size sample. In this figure we show the time evolution of the number N of vortex pairs in a square-shaped sample at $c = 0.3$ and different values of the damping parameter κ . All the curves correspond to one and the same quasi-random initial distribution of 10 pinned vortices and 10 pinned antivortices. Like in [15], the pinning potential for a vortex is provided by an ad hoc requirement $\psi = 0$ on a single

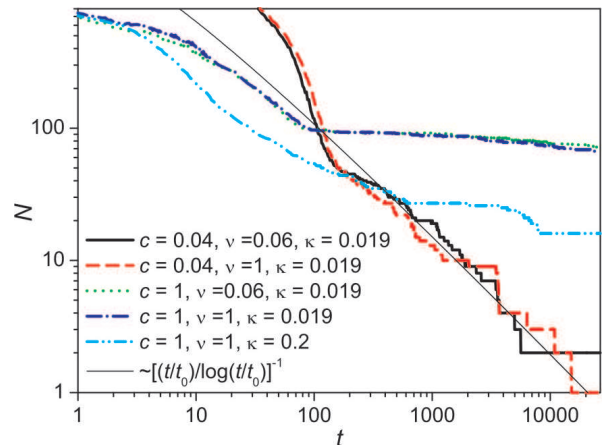


FIG. 1. Number of vortex pairs per unit cell as a function of time in a periodic system with period $L_x = L_y = 165$ at different values of c , ν , and κ (thick lines). The calculations are performed with the uniform pumping $p \equiv 1$ and grid step $h = 0.55$. The thin line corresponds to a decay $\sim [(t/t_0)/\log(t/t_0)]^{-1}$ with $t_0 = 0.33$.

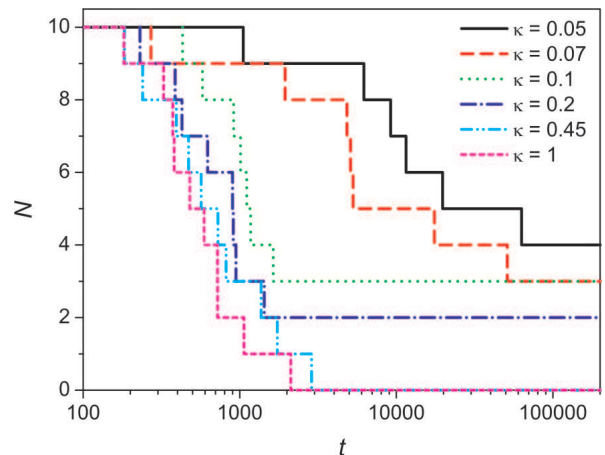


FIG. 2. Number of vortex pairs as a function of time in a square with sides $L_x = L_y = 150$ at $\nu = 1$, $c = 0.3$ and different values of κ . The calculations are performed with the Dirichlet boundary conditions, uniform pumping ($p \equiv 1$) and grid step $h = 0.5$.

point of the numerical grid, starting from an initial condition with unit circulation (clockwise or counterclockwise). At the time moment $t = 0$ this pinning potential is removed so that vortex motion and annihilation processes become possible.

As seen from Fig. 2, a decrease of the damping parameter κ leads to a decrease of the average annihilation rate for vortices and antivortices that is especially pronounced at $\kappa < 0.1$. This behavior reflects a competition between the vortex-antivortex repulsion, caused by the outflow of condensate particles from a vortex core, and the attraction due to Magnus forces, which are quite strong at $\kappa \sim 1$ but become small at $\kappa < 0.1$.

More interestingly, Fig. 2 implies that at relatively small values of κ the evolution of the system does not lead directly to a vortex-free state. Instead, metastable vortex-antivortex states are formed, where the number of vortex pairs tends to increase with decreasing κ . In the next section we consider those states in more detail.

IV. METASTABLE VORTEX-ANTIVORTEX STATES

Two examples of metastable vortex-antivortex patterns are shown in Fig. 3. Panels (a) and (b) correspond to the dash-dotted line in Fig. 2 ($\kappa = 0.2$), where two vortex-antivortex pairs remain at long times; panels (c) and (d) correspond to the dashed line ($\kappa = 0.07$) with three remaining pairs. The upper panels show the condensate density and in the lower panels the x component of the current density $\mathbf{j} = \text{Im}(\psi^* \nabla \psi)$ is plotted. The patterns of $j_x(x, y)$ allow one to easily distinguish between clockwise and counterclockwise vortices. The geometry of the shown vortex configurations is mainly determined by an interplay of the vortex-(anti)vortex repulsive interactions and the repulsion of vortices of both polarities by the sample boundaries. Since the vortex-vortex repulsion is stronger than that for a vortex and antivortex [15], minimization of the energy requires, first of all, maximum possible distances between vortices of the same chirality. The optimal distance between neighboring vortices of opposite chirality appears smaller, because a reduction of the distance between a vortex and an antivortex leads to a more efficient (though, of course, partial) mutual cancelation of their circulating currents. As a result, the obtained metastable configurations often look to be built of preformed vortex-antivortex pairs.

While the highly symmetric metastable patterns shown in Fig. 3 are fully static, at $\kappa = 0.1$ and 0.05 the evolution of the multivortex system, considered above, leads to the formation of less symmetric oscillating or rotating vortex-antivortex configurations. This is illustrated by Fig. 4, where we show, together with snapshots of the particle-density and current-density distributions, also the plots of the parameter

$$S(x, y) = \sqrt{\frac{1}{t_2 - t_1} \int_{t_1}^{t_2} dt \left(\frac{\partial |\psi(x, y, t)|^2}{\partial t} \right)^2}, \quad (5)$$

which allows to visualize trajectories of moving vortices [35]. For static vortex configurations the values of S vanish. The S -distribution displayed in Fig. 4(c) corresponds to vibrational motion in a “vortex molecule” formed by 3 vortex pairs [Figs. 4(a) and (b)]. Rotation of a 4-pair vortex configuration [Figs. 4(d) and (e)] is reflected in Fig. 4(f). As implied by the shape of the vortex trajectories, this rotation is accompanied by some confinement-induced deformations of the “vortex molecule”.

Our simulations show that formation of various metastable vortex-antivortex states is possible for a

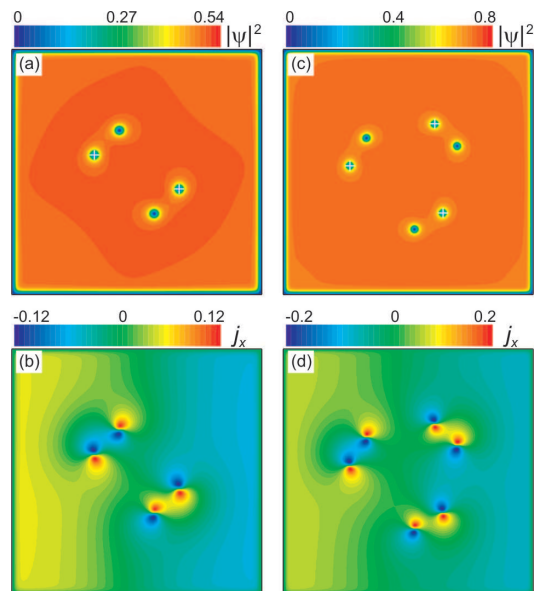


FIG. 3. Distributions of the particle density [panels (a) and (c)] and the x component of the current density [panels (b) and (d)] corresponding to the static metastable configurations of vortex pairs formed in a square with $L_x = L_y = 150$, $\nu = 1$ and $c = 0.3$ at $\kappa = 0.2$ [panels (a) and (b)] and $\kappa = 0.07$ [panels (c) and (d)]. The calculations are performed with the Dirichlet boundary conditions, uniform pumping ($p \equiv 1$) and grid step $h = 0.5$. The white crosses in panels (a) and (c) indicate vortices with counterclockwise circulating currents.

rather wide range of the sample parameters. Few examples of the obtained static vortex configurations are given below. In all the cases, the simulations start with a relatively large (40 to 100) number of pairs of vortices and antivortices, pinned at random positions within the sample. After removing the pinning potentials, the subsequent relaxation of the system is simulated until a metastable state is reached and its stability is confirmed (in particular, by the corresponding behavior of the parameter S).

Figure 5(a) demonstrates a metastable vortex-antivortex configuration, formed in a disk with a highly nonequilibrium polariton condensate ($c = 1$). At such a large value of the non-equilibrium parameter, the inward currents from the boundaries of the sample strongly push vortices to the center of the disk. This results in the formation of a rather compact vortex cluster, consisting of a relatively small number of vortex pairs.

It is obvious that the distribution of the confining inward currents and hence the sample geometry can strongly affect the shape of metastable clusters. This is illustrated by Fig. 5(b), where we show a “diamond-like” cluster stabilized as a result of vortex relaxation in a square with sizes $L_x = L_y = 100$. Due to the use of non-uniform pumping with a reduced intensity at the sample edges [$\alpha = 0.25$ and $d_0 = 0.6$ in Eq. (4)], the compressive effect of the inward currents is somewhat weakened so that the formed cluster is relatively sparse

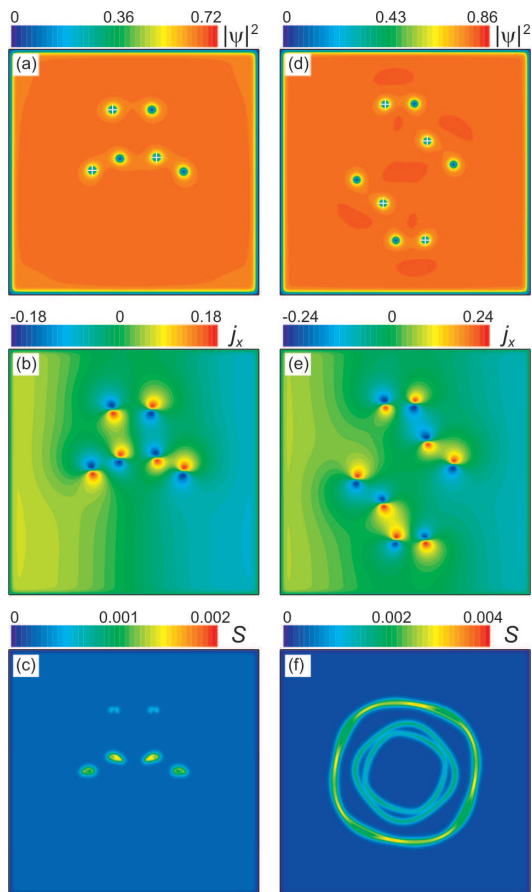


FIG. 4. Oscillating [panels (a) to (c)] and rotating [panels (d) to (f)] metastable configurations of vortex pairs formed in a square with $L_x = L_y = 150$, $\nu = 1$ and $c = 0.3$ at $\kappa = 0.1$ and $\kappa = 0.05$, respectively. The plots show snapshots of the particle-density [panels (a) and (d)] and current-density [panels (b) and (e)] distributions as well as the distributions of the parameter S with $t_2 - t_1 = 6000$ [panel (c)] and $t_2 - t_1 = 20000$ [panel (f)]. The calculations are performed with the Dirichlet boundary conditions, uniform pumping ($p \equiv 1$) and grid step $h = 0.5$. The white crosses in panels (a) and (d) indicate vortices with counterclockwise circulating currents.

despite of a rather large value of the nonequilibrium parameter ($c = 0.8$). The highly symmetric diamond-like shape of the vortex cluster, shown in Fig. 5(b), persists under a relatively strong increase of the confining currents from the sample boundaries. In the simulations, reflected in Fig. 5, such an increase has been realized by increasing c with the step $\delta c = 0.1$, starting from the configuration displayed in Fig. 5(b), at fixed values of α and d_0 . After each jump of c , its value remained constant until the order parameter relaxed to the corresponding new metastable state. As seen from Figs. 5(b) to (d), despite of a gradual compression of the cluster with increasing c , its shape is preserved even at c as large as 3.1. Similar cluster configuration and the same trends have been obtained, starting with random distributions of a relatively large number of vortex pairs, for different

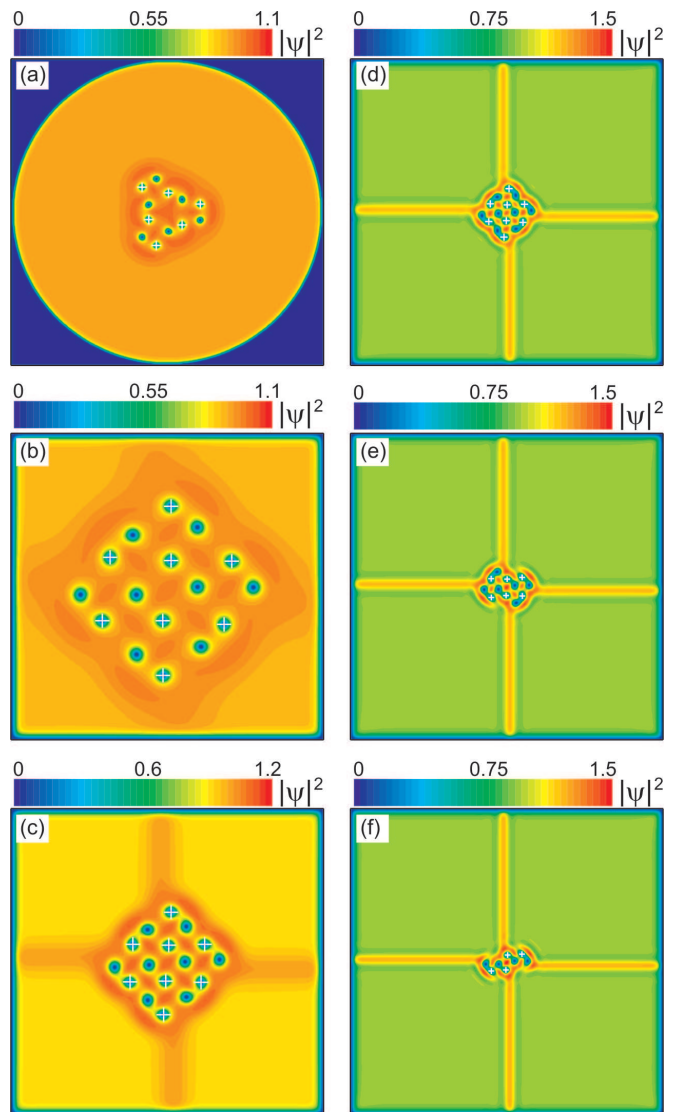


FIG. 5. (a) Cluster of 6 vortex pairs formed under uniform pumping ($p \equiv 1$) in a disk of radius $R = 100$ at $\nu = 1$, $c = 1$ and $\kappa = 0.05$. (b)-(f) Clusters of vortex pairs in a square with sides $L_x = L_y = 100$ at $\nu = 1$, $\kappa = 0.05$ and different values of c : 0.8 (b), 1.3 (c), 3.1 (d), 3.2 (e), and 3.6 (f). The pumping intensity is described by Eq. (4) with $\alpha = 0.25$ and $d_0 = 0.6$. All the calculations are performed with the Dirichlet boundary conditions and grid step $h = 0.5$. The white crosses indicate vortices with counterclockwise circulating currents.

fixed values of c ($c = 0.7, 1, 1.5, 2$) and the same set of other relevant parameters as well as for $c = 1$ and 1.5 and a two times larger sample ($L_x = L_y = 200$). At larger c , some of the vortex pairs recombine, and smaller vortex clusters are stabilized [see Figs. 5(e) and (f)] until the vortex-free state is established at $c \approx 4.5$. Besides a gradual compression of the vortex cluster, increasing inward currents from the boundaries lead also to the appearance of bulging vertical and horizontal stripes in the density of the condensate. One may notice that the vortex-antivortex configuration in Fig. 5(f) resembles

that in Fig. 4(d). However, the former is fully static: at $c = 3.6$, shape-induced anisotropy of the confining currents and the resulting anisotropy in the particle-density distribution are sufficiently strong to prevent any changes in the orientation of the “vortex molecule”.

As implied by Figs. 5(b) to (f), when increasing the nonequilibrium parameter c alone, the compressive effect, exerted on a multivortex system by the inward currents from the sample boundaries, increases more than the vortex-(anti)vortex repulsion, caused by the radial currents from vortex cores. As a result, the number of vortex pairs in the vortex cluster gradually decreases. This does not mean, however, that strong deviations from equilibrium inevitably impede formation of metastable vortex-antivortex states with large numbers of vortex pairs. Indeed, excessively strong currents from the sample boundaries can be reduced, e.g., by increasing the width d_0 of the periphery regions with partially suppressed pumping intensity [see Eq. (4)]. In Fig. 6 we show the metastable vortex configurations obtained in the corresponding simulations. As further seen from this figure, the number N of vortex pairs in the metastable states, formed as a result of vortex relaxation, tends to increase with increasing c , provided that the inward currents from the sample boundaries are appropriately tuned. This suggests that relatively large “vortex-antivortex lattices” (possibly distorted due to inhomogeneity and shape-induced anisotropy of confining currents) can be stabilized in strongly nonequilibrium polariton condensates.

V. VORTEX-ANTIVORTEX PAIR GENERATION

Let us turn to the last two questions raised in Sec. I: what happens with self-accelerated vortices when further increasing the deviation from equilibrium and can they produce new vortex-antivortex pairs? We start with the case of a single vortex at a rather large value of the nonequilibrium parameter, $c = 4$. Initially, the vortex is pinned to a random position in a finite-size square-shaped sample [see Fig. 7(a)]. At $t = 0$ the pinning potential is removed and, due to the combined effect of inward currents for the sample boundaries and self-acceleration [15], the vortex starts to move towards the left-hand-side edge of the sample [Figs.7(b) and (c)]. When approaching the edge, the relative velocity of the vortex core with respect to the inward particle flow from the boundary strongly increases, the vortex deforms [Figs.7(c) and (d)], and eventually a new vortex pair is nucleated [Figs.7(e) and (f)] and spatially separated due to vortex-(anti)vortex repulsion [Fig.7(g)]. Then all the three topological defects are dragged away from the edge by the confining current flow [Fig.7(h)].

Qualitatively, the aforescribed process may resemble vortex pair generation induced by a fast moving obstacle in superfluids [18–20] or by a defect surrounded by a supercurrent in superconductors [29, 36]. In the present

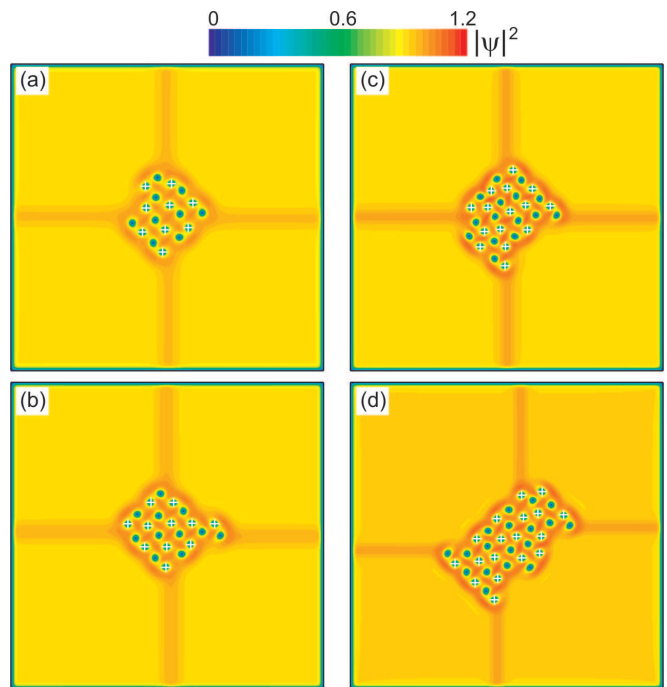


FIG. 6. Clusters with different number of vortex pairs N in a square with sides $L_x = L_y = 200$ at $\nu = 1$, $\kappa = 0.05$ and $\alpha = 0.25$: $N = 9$ for $c = 1$, $d_0 = 0.6$ (a), $N = 11$ for $c = 1.2$, $d_0 = 0.8$ (b), $N = 15$ for $c = 1.4$, $d_0 = 0.9$ (c), $N = 18$ for $c = 1.5$, $d_0 = 1$ (d). The calculations are performed with the Dirichlet boundary conditions, pumping intensity described by Eq. (4), and grid step $h = 0.5$. The white crosses indicate a vortex with counterclockwise circulating currents.

case, however, the “defect” itself produces circulating and radial currents. This makes the process of new pair formation a bit more complicated. Due to an interplay of different currents, an additional suppression of the particle density develops in front of the moving vortex core [see Fig.7(d)]. In order to bypass the resulting “defect” of a complex shape, the particle flow is redistributed and the corresponding current crowding at the edges of the defect ultimately leads to the nucleation of a new vortex pair.

Collision with the sample boundary is not the only possible source of vortex pair generation by fast moving vortices. In Fig. 8 we present the results of simulations for a (boundaryless) periodic system, which initially contains one pinned vortex-antivortex pair in a unit cell. After depinning, the vortex and antivortex move along the trajectories shown in Fig. 8(a). Further dynamics of the system is represented by few snapshots of the particle density distribution in Figs. 8(b) to (f). As seen from Fig. 8(d), the vortex-antivortex collision is accompanied by the formation of two regions with strongly suppressed density $|\psi|^2$ in-between the vortex and antivortex cores [cp. Fig. 7(d)]. Similarly to the case of the vortex-boundary collision, these suppressions rapidly evolve into new vortex-antivortex pairs [see Figs. 8(e) and (f)].

In Fig. 9(a), we show the dynamics of the number of

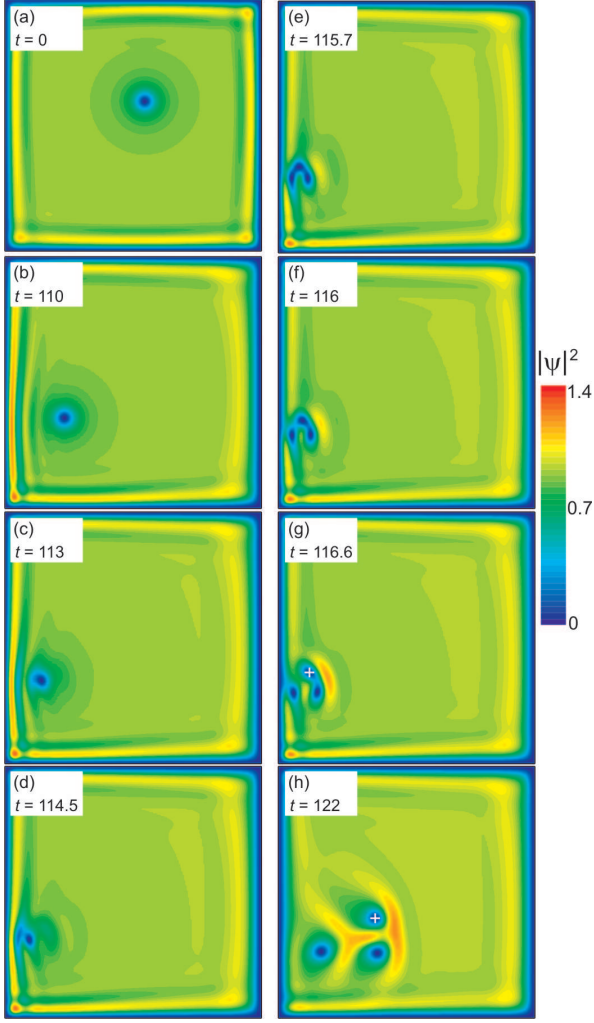


FIG. 7. Snapshots of the density distribution in a square with sides $L_x = L_y = 40$ at $c = 4$, $\nu = 1$, $\kappa = 0.01$, $\alpha = 0.4$, and $d_0 = 1.3$ for different time t after depinning of a vortex. The white crosses indicate vortices with counterclockwise circulating currents. The calculations are performed with the Dirichlet boundary conditions, pumping intensity described by Eq. (4), and grid step $h = 0.2$.

vortex pairs in the system under consideration on a relatively long time scale. As implied by the fluctuating behavior of $N(t)$ in Fig. 9(a), vortex-antivortex collisions do not necessarily lead to the generation of new vortex pairs. Very often, the result of those collisions is more “traditional”: the colliding vortex and antivortex simply annihilate.

A more detailed analysis of the simulated vortex dynamics shows that the generation of a vortex pair is more likely for higher total current between the vortex and the antivortex. Sufficiently high currents are reached only when the mean velocity of the vortex cores is in the same direction as the circulating currents between vortex and antivortex. For this reason, vortex-vortex collisions, where the circulating currents between them are in op-

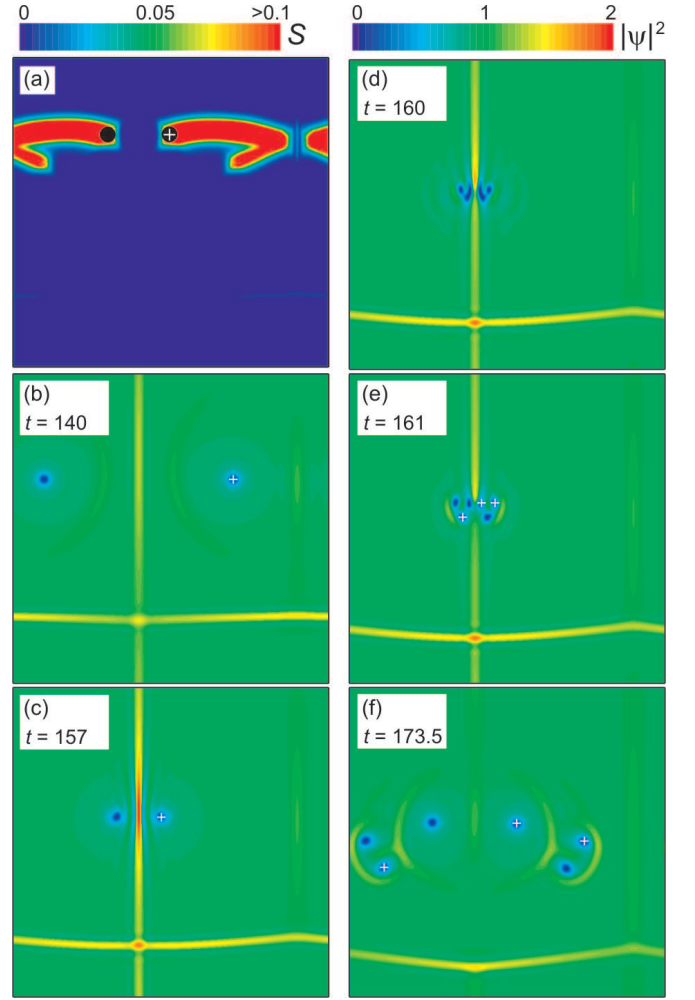


FIG. 8. Vortex dynamics in a unit cell of a periodic system with period $L_x = L_y = 80$ at $c = 4$, $\nu = 1$, and $\kappa = 0.01$. (a) Parameter S for the time interval from the moment of depinning of a vortex-antivortex pair ($t_1 = 0$) to $t_2 = 140$. The initial positions of the vortex and antivortex are indicated with the black circles. (b)-(f) Snapshots of the density distribution for different time t after depinning. The white crosses indicate vortices with counterclockwise circulating currents. The calculations are performed with the uniform pumping intensity $p \equiv 1$ and grid step $h = 0.2$.

posite directions, do not produce additional vortices.

The condition for vortex pair generation is fulfilled, e.g., in the situation displayed in Figs. 8(b) to (d). Another example of this kind is the collision of the vortex and antivortex, which are shown inside the white rectangular frame in Fig. 9(b). Interestingly, four rather than two new vortex pairs nucleate as a result of this collision [see Fig. 9(c)]. However, three of them recombine within a relatively short time interval [Fig. 9(d)]. For the vortex-antivortex pair, shown inside the dashed circle in Fig. 9(b), the above condition is violated and this pair annihilates [see Figs. 9(c) to (e)]. A vortex-antivortex collision violating the above condition is evidenced also by the shape the vortex trajectories in Fig. 8(a). In this

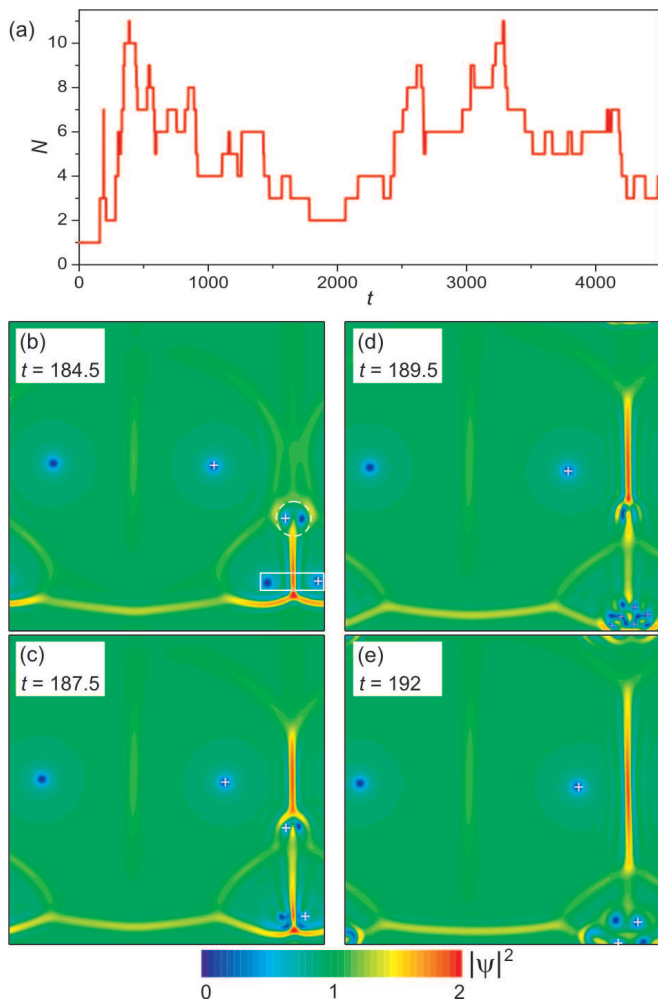


FIG. 9. (a) Number of vortex pairs per unit cell as a function of time in a periodic system with period $L_x = L_y = 80$ at $c = 4$, $\nu = 1$, and $\kappa = 0.01$. (b)-(e) Snapshots of the density distribution for different time t after depinning of the initially present vortex-antivortex pair. The white crosses indicate vortices with counterclockwise circulating currents. The vortex and antivortex, shown inside the white dotted circle in panel (a), further annihilate as a result of their collision. The collision between the vortex and antivortex, shown inside the white solid-line rectangle in panel (a), leads to production of new vortex pairs. The calculations are performed with the uniform pumping intensity $p \equiv 1$ and grid step $h = 0.2$.

case, the vortex and antivortex are simply “scattered” by each other due to mutual repulsion.

In a highly nonequilibrium polariton condensate, due to the presence of strong radial flows, emitted from vortex cores, in combination with a relatively slow relaxation of the flow fields [15], vortex motion often lead to the appearance of pronounced time-dependent inhomogeneities in the current and density distributions. An example can be seen in the formation of density “bulges” in front of fast moving vortices [see Figs. 7(g) and (h)]. Our simulations show that vortex pair generation can occur also as a result of vortex interaction with those inhomogeneities.

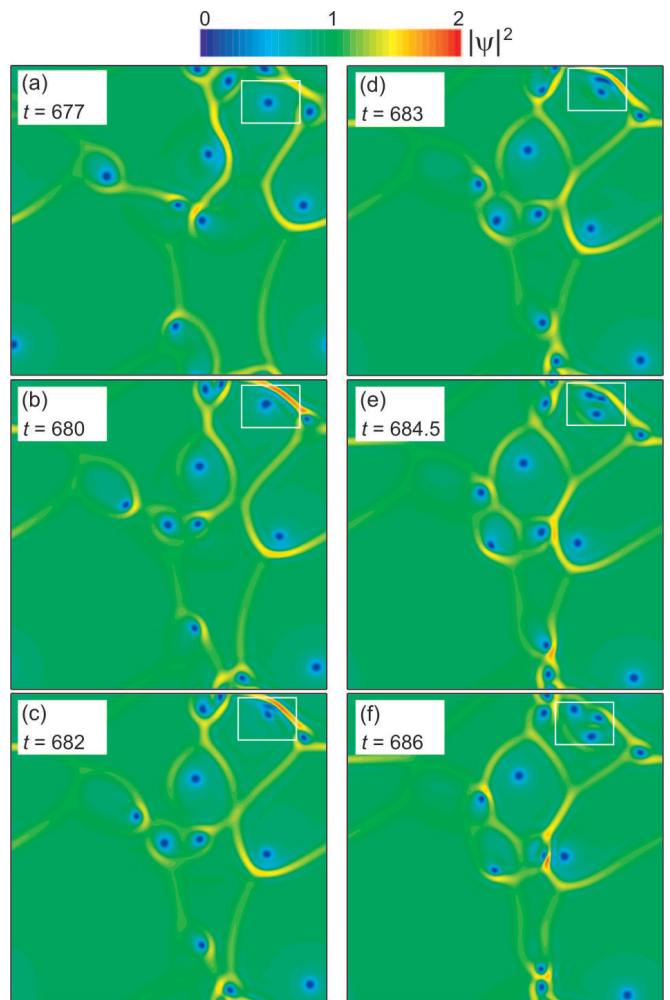


FIG. 10. Six snapshots of the density distribution for different time t after depinning of the initially present vortex-antivortex pair in a periodic system with period $L_x = L_y = 80$ at $c = 4$, $\nu = 1$, and $\kappa = 0.01$. The white solid-line rectangles indicate the region where a fast moving vortex produces a new vortex-antivortex pair. The calculations are performed with the uniform pumping intensity $p \equiv 1$ and grid step $h = 0.2$.

This effect is illustrated in Fig. 10. The vortex, which moves in the region indicated with the white rectangle [see Figs. 10(a) and (b)], generates a new vortex pair when approaching a density bulge [Figs. 10(c) to (f)]. Remarkably, the growth of this bulge is seen to be caused, to a great extent, by the fast motion of the same vortex [compare Fig. 10(b) to Fig. 10(a)]. The shape of the curve $N(t)$ in Fig. 9(a), where the jumps with an increase of N by 1 predominate, implies that the aforescribed mechanism of vortex pair generation may be very efficient in multivortex systems.

It should be mentioned that in our simulations, performed for a relatively wide range of parameters, we did not meet the situation where a moving vortex would produce a fully developed “vortex-antivortex street”. Still we do not completely exclude the possibility that such

a process can be realized under certain – maybe rather exotic – conditions.

VI. CONCLUSIONS

We have numerically studied the dynamics of multivortex systems in nonequilibrium quantum fluids described by the gGPE. It is shown that, when moving away from equilibrium, the rate of vortex-antivortex annihilation in these systems strongly decreases due to an enhancement of the repulsive component in the vortex-antivortex interaction.

In parallel with infinite periodic systems we have considered also finite-size samples with the Dirichlet boundary conditions, where vortex confinement is provided by the inward currents flowing from the sample edges. In the case of weak damping, relaxation of multivortex systems in those samples typically leads – instead of full annihilation of vortex pairs – to the formation of metastable vortex-antivortex clusters. The shape and size of these clusters are determined by an interplay of the confining currents and vortex-(anti)vortex repulsive interactions. Since the vortex-antivortex repulsion is weaker

than that between vortices of the same chirality, relatively small and sparse clusters, obtained at moderate deviations from equilibrium, often look to consist of preformed “bound” vortex-antivortex pairs. The internal structure of bigger and denser clusters, formed at larger values of the nonequilibrium parameter, more resembles a vortex-antivortex lattice, somewhat distorted due to (in general, anisotropic) compressive effect of the confining currents.

We have also demonstrated that, at strong nonequilibrium, self-accelerated vortices can induce generation of vortex pairs. Thus, pair-production processes happen when a self-accelerated vortex moves in a spatially inhomogeneous counterflow of particles. Such a situation is realized, in particular, for vortices approaching sample boundaries. Another striking example is the appearance of two or more new vortex pairs as a result of a vortex-antivortex collision.

ACKNOWLEDGEMENTS

We thank Sebastian Diehl for a stimulating discussion. This work was financially supported by the FWO Odysseus program.

-
- [1] P. M. Chaikin, *Principles of Condensed Matter Physics* (Cambridge University Press, Cambridge, 2000).
- [2] I. Carusotto and C. Ciuti, *Rev. Mod. Phys.* **85**, 299 (2013).
- [3] J. Kasprzak, M. Richard, S. Kundermann, A. Baas, P. Jeambrun, J. Keeling, F. Marchetti, M. Szymańska, R. Andre, J. Staehli, V. Savona, P. B. Littlewood, B. Deveaud and Le Si Dang, *Nature* **443**, 409 (2006).
- [4] K. G. Lagoudakis, M. Wouters, M. Richard, A. Baas, I. Carusotto, R. André, L. S. Dang, and B. Deveaud-Plédran, *Nat. Phys.* **4**, 706 (2008).
- [5] K. G. Lagoudakis, F. Manni, B. Pietka, M. Wouters, T. C. H. Liew, V. Savona, A. V. Kavokin, R. André, and B. Deveaud-Plédran, *Phys. Rev. Lett.* **106**, 115301 (2011).
- [6] D. Caputo, D. Ballarini, G. Dagvadorj, C. S. Muñoz, M. De Giorgi, L. Dominici, K. West, L. N. Pfeiffer, G. Gigli, F. P. Laussy, M. H. Szymańska and D. Sanvitto, *Nat. Mat.* **17**, 145 (2018).
- [7] T. C. H. Liew, O. A. Egorov, M. Matuszewski, O. Kyriienko, X. Ma, and E. A. Ostrovskaya, *Phys. Rev. B* **91**, 085413 (2015).
- [8] F. M. Marchetti, M. H. Szymańska, C. Tejedor, and D. M. Whittaker, *Phys. Rev. Lett.* **105**, 063902 (2010).
- [9] E. Cancellieri, T. Boulier, R. Hivet, D. Ballarini, D. Sanvitto, M. H. Szymanska, C. Ciuti, E. Giacobino, and A. Bramati, *Phys. Rev. B* **90**, (2014).
- [10] X. Ma and S. Schumacher, *Phys. Rev. B*, 235301 (2017).
- [11] G. Dagvadorj, J. M. Fellows, S. Matyjaśkiewicz, F. Marchetti, I. Carusotto, and M. H. Szymańska, *Phys. Rev. X* **5**, 041028 (2015).
- [12] G. Wachtel, L. M. Sieberer, S. Diehl and E. Altman, *Phys. Rev. B* **94**, 104520 (2016).
- [13] L. M. Sieberer, G. Wachtel, E. Altman and S. Diehl, *Phys. Rev. B* **94**, 104521 (2016).
- [14] A. Zamora, L. M. Sieberer, K. Dunnett, S. Diehl, and M. H. Szymańska, *Phys. Rev. X* **7**, 041006 (2017).
- [15] V. N. Gladilin and M. Wouters, *New J. Phys.* **19**, 105005 (2017).
- [16] M. Kulczykowski and M. Matuszewski, *Phys. Rev. B* **95**, 075306 (2017).
- [17] M. Matuszewski and E. Witkowska, *Phys. Rev. B* **89**, 155318 (2014).
- [18] K. Sasaki, N. Suzuki, H. Saito, *Phys. Rev. Lett.* **104**, 150404 (2010).
- [19] W. J. Kwon, J. H. Kim, S. W. Seo, Y. Shin, *Phys. Rev. Lett.* **117**, 245301 (2016).
- [20] H. Saito, T. Aioi, and T. Kadokura, *Phys. Rev. B* **86**, 014504 (2012).
- [21] M. Wouters and I. Carusotto, *Phys. Rev. Lett.* **99**, 140402 (2007).
- [22] J. Keeling and N. G. Berloff, *Phys. Rev. Lett.* **100**, 250401 (2008).
- [23] N. Bobrovska and M. Matuszewski, *Phys. Rev. B* **92**, 035311 (2015).
- [24] L.P. Pitaevskii, *Zh. Eksp. Teor. Fiz.* **35**, 408 (1958) [*Sov. Phys. JETP* **35**, 282 (1959)].
- [25] M. Wouters, *New J. Phys.* **14**, 075020 (2012).
- [26] A. V. Silhanek, V. N. Gladilin, J. Van de Vondel, B. Raes, G. W. Ataklti, W. Gillijns, J. Tempere, J. T. Devreese and V. V. Moshchalkov, *Supercond. Sci. Technol.* **24**, 024007 (2011).

- [27] J. Van de Vondel, V. N. Gladilin, A. V. Silhanek, W. Gillijns, J. Tempere, J. T. Devreese, and V. V. Moshchalkov, *Phys. Rev. Lett.* **106**, 137003 (2011).
- [28] J.-Y. Ge, V. N. Gladilin, J. Tempere, C. Xue, J. T. Devreese, J. Van de Vondel, Y. Zhou, and V. V. Moshchalkov, *Nat. Commun.* **7**, 13880 (2016).
- [29] J.-Y. Ge, V. N. Gladilin, J. Tempere, J. T. Devreese, and V. V. Moshchalkov, *Nano Lett.* **17**, 5003 (2017).
- [30] G. Tosi, F. M. Marchetti, D. Sanvitto, C. Antón, M. H. Szymańska, A. Berceanu, C. Tejedor, L. Marrucci, A. Lemaitre, J. Bloch, and L. Viña, *Phys. Rev. Lett.* **107**, 036401 (2011).
- [31] F. M. Marchetti, M. H. Szymańska, C. Tejedor, and D. M. Whittaker, *Phys. Rev. Lett.* **105**, 063902 (2010).
- [32] R. Dall, M. D. Fraser, A. S. Desyatnikov, G. Li, S. Brodbeck, M. Kamp, C. Schneider, S. Hfling, and E. A. Ostrovskaia, *Phys. Rev. Lett.* **113**, 200404 (2014).
- [33] K. G. Lagoudakis, F. Manni, B. Pietka, M. Wouters, T. C. H. Liew, V. Savona, A. V. Kavokin, R. André and B. Deveaud-Plédran, *Phys. Rev. Lett.* **106**, 115301 (2011).
- [34] P. Comaron, G. Dagvadorj, A. Zamora, I. Carusotto, N. P. Proukakis, M. H. Szymanska, *Phys. Rev. Lett.* **121**, 095302 (2018).
- [35] V. N. Gladilin, J. Tempere, J. T. Devreese, W. Gillijns and V. V. Moshchalkov, *Phys. Rev. B* **80** 054503 (2009).
- [36] J.-Y. Ge, J. Gutierrez, V. N. Gladilin, J. T. Devreese, V. V. Moshchalkov, *Nat. Commun.* **6**, 6573 (2015).